

Design and performance study of a parametric diverterless supersonic inlet

Eiman B Saheby¹ , Xing Shen² and Anthony P Hays³

Proc IMechE Part G:
J Aerospace Engineering
0(0) 1–20
© IMechE 2019
Article reuse guidelines:
sagepub.com/journals-permissions
DOI: 10.1177/0954410019875384
journals.sagepub.com/home/pig



Abstract

Diverterless supersonic inlet integration for a flight vehicle requires a three-dimensional compression surface (bump) design with an acceptable shock structure and boundary layer diversion; this results in a low drag induction system with acceptable propulsive efficiency. In this investigation, a computational fluid dynamics-based-generated bump is used to design an integrated diverterless supersonic inlet without any bleed mechanism on a forebody with a large wetted area. Numerical solution of the Navier–Stokes equations simulates the flow pattern of the configuration. The forebody design analysis includes simulating the effects of angle of attack and sideslip by dependent computational domains. Results demonstrate the ability of the bump surface to keep the shock structures in an operational mode even at high supersonic angles of attack. Analysis of shock structures and shock wave boundary layer interactions at supersonic maneuver conditions indicate that the aerodynamic efficiency of the diverterless supersonic inlet in conditions with a thick boundary layer and high angles of attack is sufficient to ensure operation throughout the supersonic flight envelope.

Keywords

Diverterless supersonic inlet, upstream boundary layer, highly integrated inlet, effects of forebody, parametric compression surface, bump surface, shock wave boundary layer interactions, forebody–inlet interactions

Date received: 16 April 2019; accepted: 3 August 2019

Introduction

Evolution of an optimum supersonic forebody configuration for reducing inlet installation drag has resulted in several different inlet designs. The most recent concept, which has drawn the attention of designers, is the diverterless supersonic inlet (DSI). The DSI is formed on the basis of a fuselage-integrated dual-purpose bump compression surface which diverts the upstream boundary layer (BL) in addition to compressing the air for the inlet. The pressure gradient (from high at the center to the low at the sides) on the bump surface diverts the low subsonic portion of the upstream BL to the sides of the bump. This flow pattern around the bump surface, without considering the inlet structure, has been investigated separately in several papers; results of a wind tunnel test in 2009 on a bump surface by Tillotson and Loth¹ show the shock pattern and BL diversion clearly at Mach 3. A paper by Lo et al.² reports the effects of jet injection into the wake region of a generic bump geometry at Mach 1.9. But the first official report of the DSI (or bump for inlet design) concept was published Simon et al.³ in 1957. In this NACA report, a forebody with bump inlet was compared with ramp inlet over a range of Mach numbers from 1.5 to 2.0 with surfaces employing BL bleed, and the results

quantified the propulsive efficiency of the DSI. The mechanical simplicity and acceptable aerodynamic performance with lower weight made it the first choice of Lockheed Martin designers of the F-35 Lightning II. Chinese designers followed the same DSI concept on the Chengdu J-20, Shenyang FC-31, and CAC/PAC JF-17 fighters. The bump surface of the DSI can be generated by applying the stream tracing technique in a known flow field after a conical shock (or shocks) which provides a robust design method.^{4–7} Figure 1 shows streamlines, released from a flat surface, which form the compression surface after passing through the conical shock. For the wave-derived bump surface, the BL diverting ability and pressure compression ratio is dictated by the conical shock (or shocks).^{5,7} This means that the design

¹College of Aerospace Engineering, Nanjing University of Aeronautics and Astronautics, Nanjing, China

²College of Aerospace Engineering, Nanjing University of Aeronautics and Astronautics, Nanjing, China

³Aircraft Design and Consulting, San Clemente, CA, USA

Corresponding author:

Xing Shen, Nanjing University of Aeronautics and Astronautics, Yudao Street 29, Nanjing, Jiangsu 210016, China.

Email: shenx@nuaa.edu.cn

framework is fixed, and changing the shock pattern is not easy, especially for low supersonic speeds. Another limitation is related to the hyperbolic intersection which results from the intersection of a plane and conical shock. The resulting intersection geometry is a hyperbolic curve, so the bump surface must be trimmed to adapt it to the inlet entrance and fuselage.⁸ This trimming means that the resulting bump is partly stream traced, so that it needs additional surfaces at the sides.

In 2000, a detailed analysis of a wave-derived bump surface was published by Yang.⁹ The paper illustrated the first results of simulations and wind

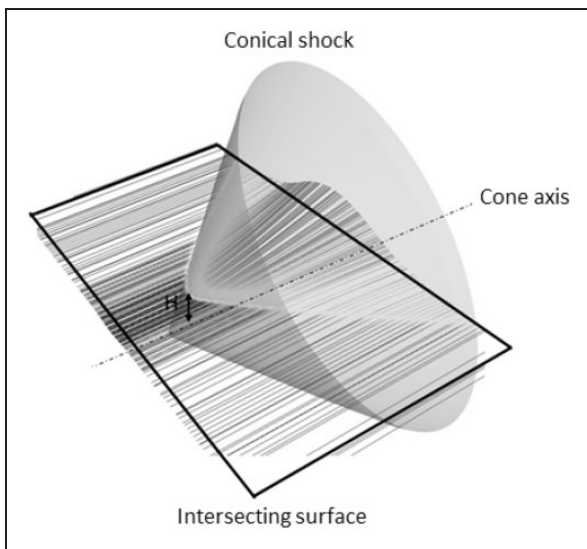


Figure 1. Classic streamline tracing method for designing the bump surface.⁸

tunnel tests of a subscale J-17 induction system. Papers about this inlet on J-17 configuration were published by J Masud and coworkers between 2010 and 2015.^{10,11} The studies show several important properties of the DSI concept, such as off-design shock patterns at the inlet entrance. Figure 2(a) shows the DSI on the J-17 and Figure 2(b) shows computational fluid dynamics (CFD) simulation of this inlet.

In addition to the stream tracing approach, it is possible to use parametric geometries for designing the bump compression surface. In this method, a set of equations define the compression surface, but finding the suitable shock pattern requires several iterations between CFD simulations and modification of the initial computer-aided design (CAD) geometry. An algorithm based on the trigonometric equations to develop such a CFD-based-design surfaces is reported in a thesis by Svensson.¹³ The algorithm shows that a three-dimensional compression surface can be optimized over a large geometric area. Also, use of a parametric bump surface as a replacement to the final compression surface of a multi-ramp supersonic inlet is reported by Sang D Kim with and without a bleed mechanism.^{14–16} The purpose of this paper is to demonstrate a design approach and efficiency analysis of a parametric DSI, operating at Mach 1.60, and without a bleed system. Flow structure over the bump surface, BL diversion, and shock wave BL interactions are investigated by considering the effects of the flow pattern generated by the forebody at different angle of attack and sideslip. The aerodynamic efficiency of the system is measured and compared with available data from other concepts.

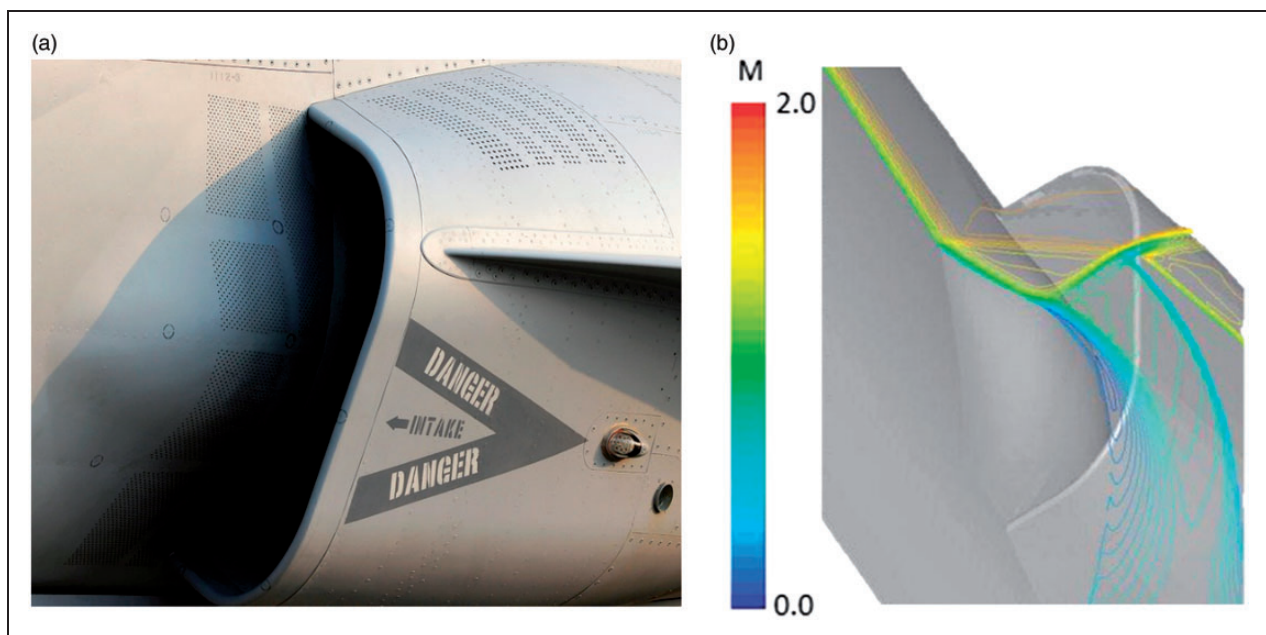


Figure 2. Stream traced DSI with trimmed hyperbolic platform. (a) DSI on J-17 Thunder¹² and (b) CFD simulation of J-17 induction system.¹⁰

Design approach and model development

Trigonometric compression surface design

Using the parametric approach, the entire bump surface can be designed using analytical geometry. The compression surface in our study is defined along its plane of symmetry by a central guide curve, shown as C_s in Figure 3(a) and a set of cross-sectional curves (C_c), constrained in a rectangular planform. All of the curves can be created by a quadratic trigonometric polynomial function^{17,18} with the formulation of

$$C_c(x) = \sum_0^3 P_i f_{i,3} \quad x \in \left[0, \frac{\pi}{2}\right], \quad \mu_C, \quad \zeta \in [-1, 1] \quad (1)$$

(see the study by Liu et al.¹⁸)

In this function, P_0, P_1, P_2 and P_3 are the control points, μ_C and ζ are the shape control variables and are the trigonometric basis of equation (1). The effects of μ_C and ζ on the curvature are investigated in the study by Liu et al.,¹⁸ but in the current design these values are equal to 1.0.

$$f_{0,3}(x) = 1 - (1 + \zeta) \sin x + \zeta \sin^2 x$$

$$f_{1,3}(x) = (1 + \zeta) \sin x - (1 + \zeta) \sin^2 x$$

$$f_{2,3}(x) = (1 + \mu_C) \sin x - (1 + \mu_C) \sin^2 x \quad (2)$$

$$f_{3,3}(x) = 1 - (1 + \mu_C) \cos x + \mu_C \cos^2 x$$

The dimensions of the rectangle and the maximum height of the compression surface can be defined based on the dimensions of the inlet entrance. According to equation (1), each curve needs to have four control points (P_0 to P_3) as shown in Figure 3(c). This figure shows a typical C_s curve in the x - z plane. P_0 and P_1 are determined by the rectangular profile; P_0 is placed on the rectangle and the coordinates of P_3 correspond to the end of the rectangle and the maximum height of the compression surface, so that the first point of each transversal curve, C_c , is located on the longitudinal segment (of rectangle), corresponds to a unique longitudinal coordinates (“ z ” in Figure 3(a)) and the last control point P_3 is on the curve C_s . By determining the longitudinal coordinate of the cross-sectional plane, the control points of C_c curves can be summarized on the cross-sectional plane as

$$x_{P_{0-C_1}} = x_{P_{0-C_2}} = \dots = x_{P_{0-C_n}}$$

$$x_{P_{3-C_1}} = x_{P_{3-C_2}} = \dots = x_{P_{3-C_n}}$$

$$y_{P_{0-C_1}} = y_{P_{0-C_2}} = \dots = y_{P_{0-C_n}} = 0$$

$$y_{P_{3-C_1}} = y_{C_{s_1}}, \quad y_{P_{3-C_2}} = y_{C_{s_2}}, \quad \dots = y_{P_{3-C_n}} = y_{C_{s_n}} \quad (3)$$

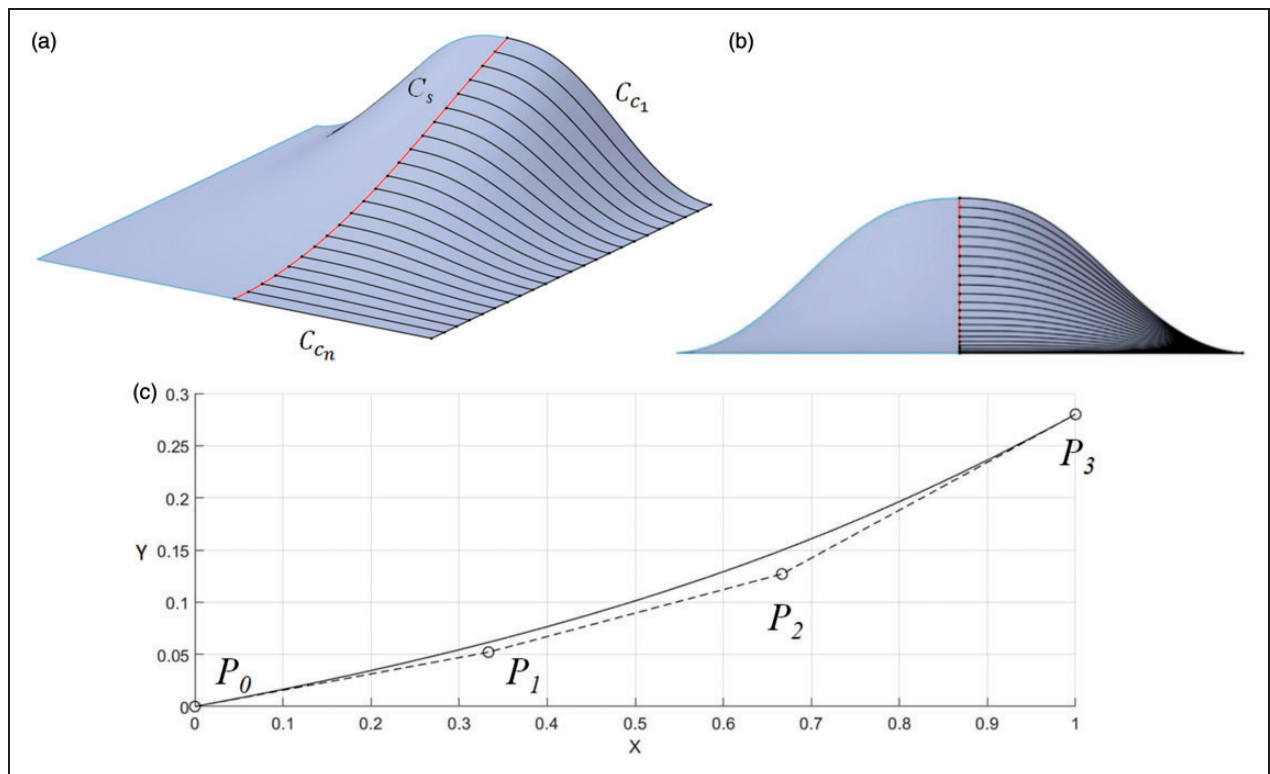


Figure 3. Surface development by trigonometric equations. (a) Perspective view, (b) front view, and (c) Typical guide curve C_s .

The $x_{P_{0-C_{1,2,\dots,n}}}$, $x_{P_{3-C_{1,2,\dots,n}}}$, $y_{P_{0-C_{1,2,\dots,n}}}$, and $y_{P_{3-C_{1,2,\dots,n}}}$ correspond to the transversal and vertical coordinates of the control points P_0 and P_3 in a determined cross-sectional planes and $y_{C_{s_{1,2,\dots,n}}}$ is the vertical coordinate of the junction points on C_s curve. Another two control points for C_c curves are determined based on the following constraints

$$\begin{aligned} x_{P_{1-C_{c_1}}} &= x_{P_{1-C_{c_2}}} = \dots = x_{P_{1-C_{c_n}}} \\ x_{P_{2-C_{c_1}}} &= x_{P_{2-C_{c_2}}} = \dots = x_{P_{2-C_{c_n}}} \\ y_{P_{1-C_{c_1}}} &= y_{P_{0-C_{c_1}}}, \quad y_{P_{1-C_{c_2}}} = y_{P_{0-C_{c_2}}}, \dots, \quad y_{P_{1-C_{c_n}}} = y_{P_{0-C_{c_n}}} \\ y_{P_{2-C_{c_1}}} &= y_{P_{3-C_{c_1}}}, \quad y_{P_{2-C_{c_2}}} = y_{P_{3-C_{c_2}}}, \dots, \quad y_{P_{2-C_{c_n}}} = y_{P_{3-C_{c_n}}} \end{aligned} \quad (4)$$

This approach reduces the variables (control points) of the surface design problem, and the final geometry becomes a function of the C_s curve. The lofting process by CAD software generates the final surface within the rectangle in Figure 3(a). The main challenge of defining the surface is in achieving the desired Mach range at or near the end of the compression surface where the normal shock is located and maximum BL diversion occurs, and this requires several iterations between the CAD finalized surfaces and CFD simulations. In contrast to two-dimensional compression surfaces, designing a bump geometry to reduce the flow velocity to the designated throat Mach number is challenging because the parametric compression surface generates a three-dimensional shock pattern with a lateral velocity gradient which is not analytically predictable, so that the flow pattern of the resulting surface must be simulated by CFD. To constrain this optimization problem, the range of the transversal Mach number distribution on the normal shock plane perpendicular to the curve C_s is selected as $1.20 < M < 1.40$. This range is widely used for throat Mach numbers of practical external compression induction systems to keep a stable terminal shock at the entrance.¹⁹ The BL diversion magnitude can be specified by the maximum lateral velocity component, U_z , on the bump surface before the normal shock wave. For bump surfaces with similar velocity gradients before the normal shock, the one with maximum U_z is the selected compression surface for inlet design. Although the BL diversion has a direct relationship to the height of the bump surface²⁰; in the current study, the height of the bump is constant but the shoulder section can be redesigned based on the length of the cowl.

Inlet model for CFD simulations

The final inlet is designed by adding the bump compression surface to a swept forward cowl and a subsonic diffuser. In this design, the forebody length and height of the cowl are fixed parameters, but the longitudinal coordinate of the cowl lip can be adjusted. In this study, an S-duct (for an engine with a high-offset from the inlet) is not considered, although it is

recognized that an S-duct may be required for low observability. This type of duct usually results in BL separation at the bends which increases the complexity of flow pattern measurement, whereas the priority of current research is the supersonic diffuser design. Solving duct flow separation problems or duct optimization is out of the scope of this study. The subsonic duct is a smooth transition between the throat cross-section and a circular outlet which is shown in Figure 4(a). The throat cross-section is defined by the bump and cowl geometries. The length to outlet diameter ratio of the subsonic diffuser L/D is 5.6. Most experimental models such as the prototypes in the earlier studies^{3,10,21} adopt similar ratios.

Two cowl concepts are designed based on the distance of the cowl lip to the oblique shock front. In Figure 4(c), the cowl of inlet A is adjusted to intersect with the first layer of the oblique shock front. Using this approach, the inlet can capture the high-loss flow at the subcritical operation mode.²² In this mode, the normal shock stands in front of the entrance with some distance to the cowl lip. According to the study by Seddon and Goldsmith,⁴ this mode of operation is usually seen on the external compression inlets for values of $M_\infty < 2.0$. The lip of cowl B is located after the oblique shock front at a location where the normal shock receives a lower Mach number in front of the cowl lip. Moving the cowl aft results in a longer curve for the shoulder section but the ducts follow the same curvature. Using inlet B, the sensitivity of supersonic performance to the shoulder section can be investigated. The cowl lip uses a geometry transition between a relatively sharp lip on the plane of symmetry and a more blunt lip close to the fuselage. Figure 4(b) shows the CAD finalized basic models. The yellow surface indicates the extension of the shoulder section of the bump.

By extending the wetted area in front of the bump, it is possible to estimate the effects of BL thickness on the performance of the DSI with a simpler computational domain,²³ but when installed on an aircraft, its forebody affects the flow pattern and thickness of the BL, especially at maneuver conditions. A simple planar extension of the wetted area does not accurately provide simulation of the airflow upstream of the bump. In order to investigate these effects, for this study, the DSI is integrated on a generic forebody shown in Figure 5.

For this forebody-inlet configuration, two planes of symmetry appear in the grid domains to reduce the computational costs in analyzing the angle of attack and sideslip effects. Table 1 shows the dimensions of the concept.

CFD simulations

Grid generations and boundary conditions

Generating the grid for a single bump compression surface is quite straightforward; the study case is

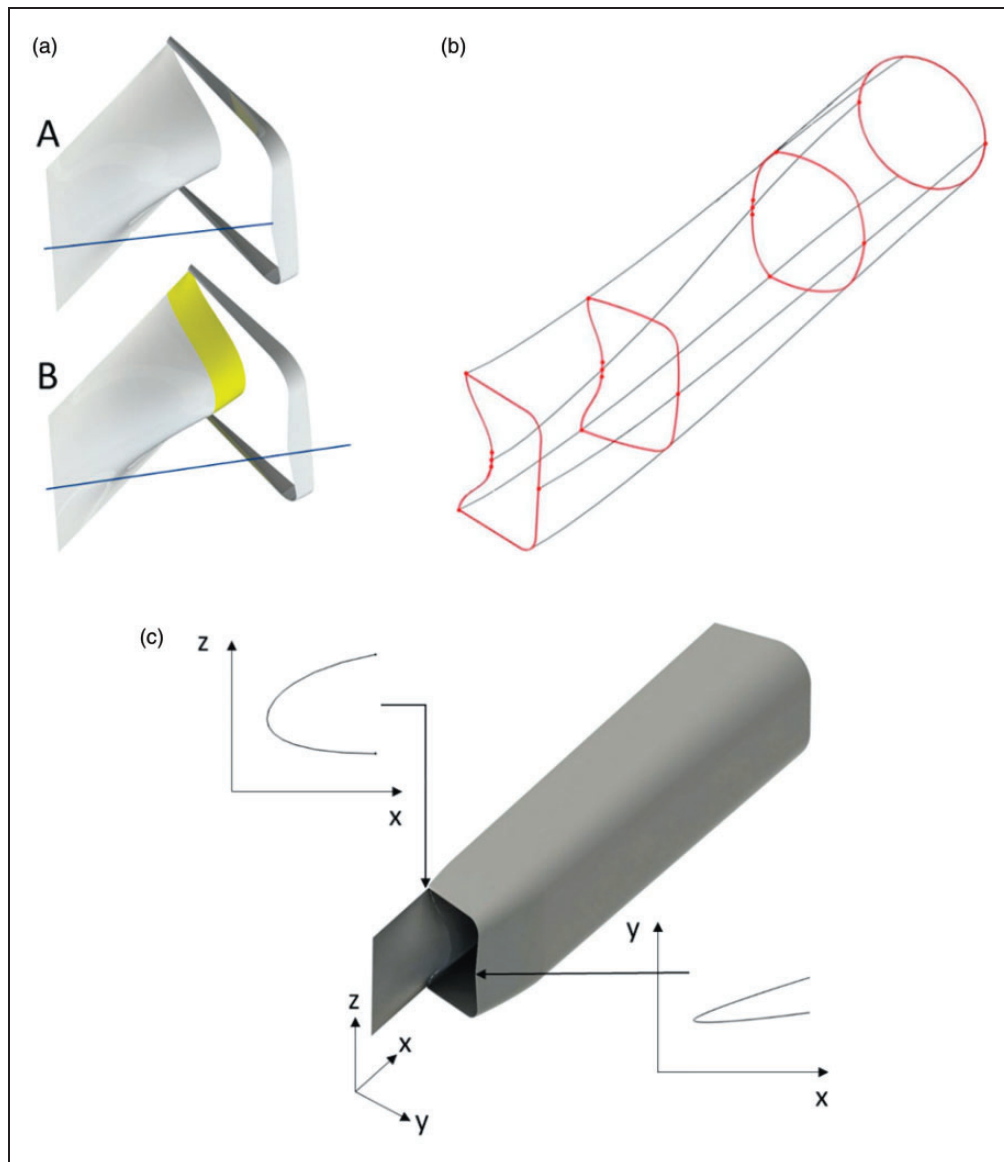


Figure 4. CAD finalized inlet. (a) Cowl geometries, (b) wire frame view of subsonic duct, and (c) CAD finalized inlet.

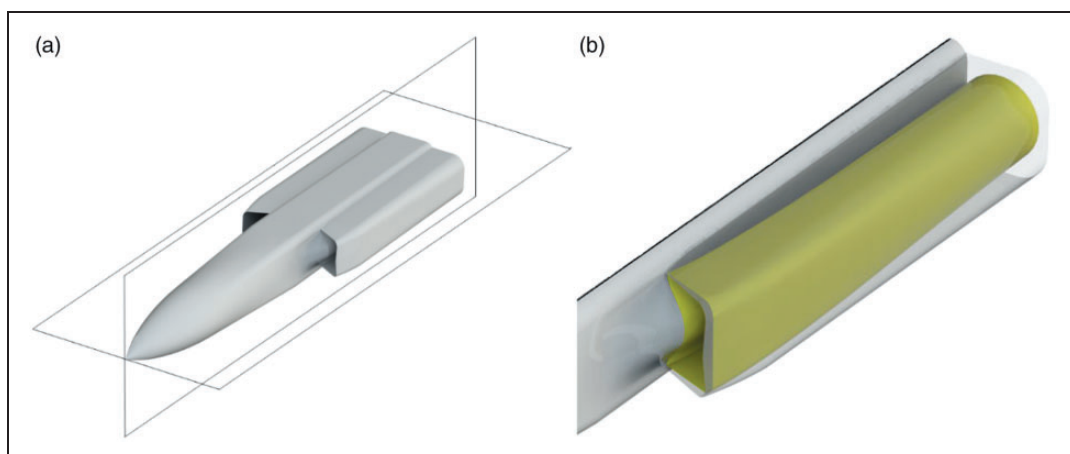


Figure 5. Forebody-inlet configuration. (a) Perspective view and (b) close up view of the inlet with transparent cowl.

symmetrical about the longitudinal vertical plane, and in order to minimize the computational costs, only half of the geometry is considered for mesh generation. For analyzing the effects of angle of attack

and sideslip on the forebody-integrated-inlet two different domains are needed based on the corresponding plane of symmetry. Although it is possible to use two symmetry boundary conditions for isolated inlets (when angle of attack and sideslip angle are both zero), in order to have an accurate estimation of the forebody effects on the internal flow pattern of the inlets, the complete inlet is used for grid generation. Figures 6 to 8 show the mesh domains, and the blue surface is the symmetry boundary condition. The grid quality parameters remain the same for all study cases; grid structure of the entrances, forebody section, and subsonic duct have the same number of cells, Y^+ , and orthogonality factor. The forebody and entrance are surrounded by pressure-farfield boundary condition which are connected to a pressure

Table 1. Specifications of the concept.

Segment	Length
	Outlet diameter
Forebody (from nose to the bump)	6.4
Length of bump	1.0
Width of bump	1.0
Height of bump	0.2
Height of cowl	0.7
Length of diffuser	5.6

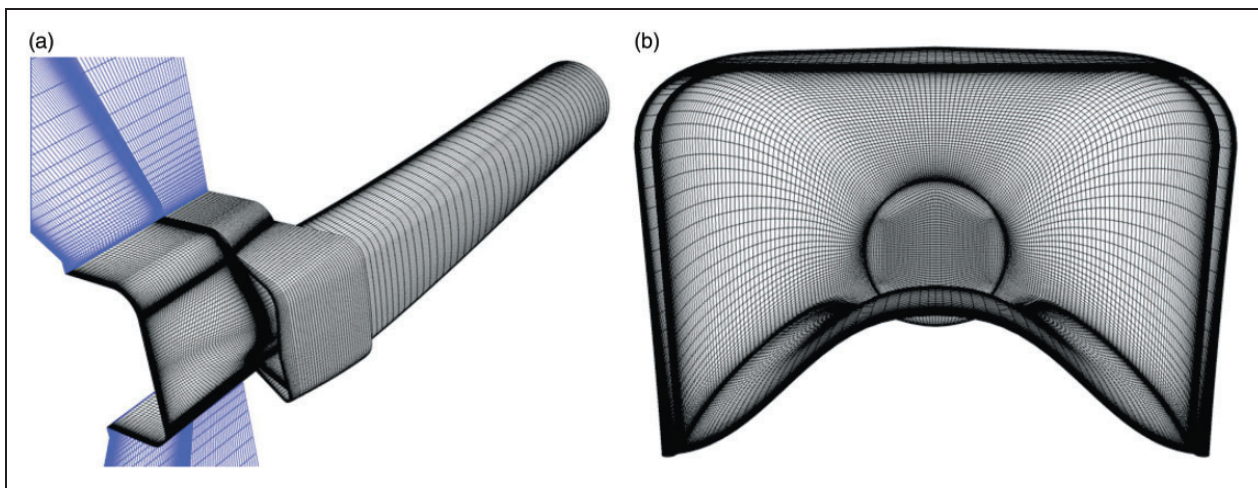


Figure 6. Mesh structure of isolated inlet. (a) Surface grid and (b) perspective front view of the subsonic duct.

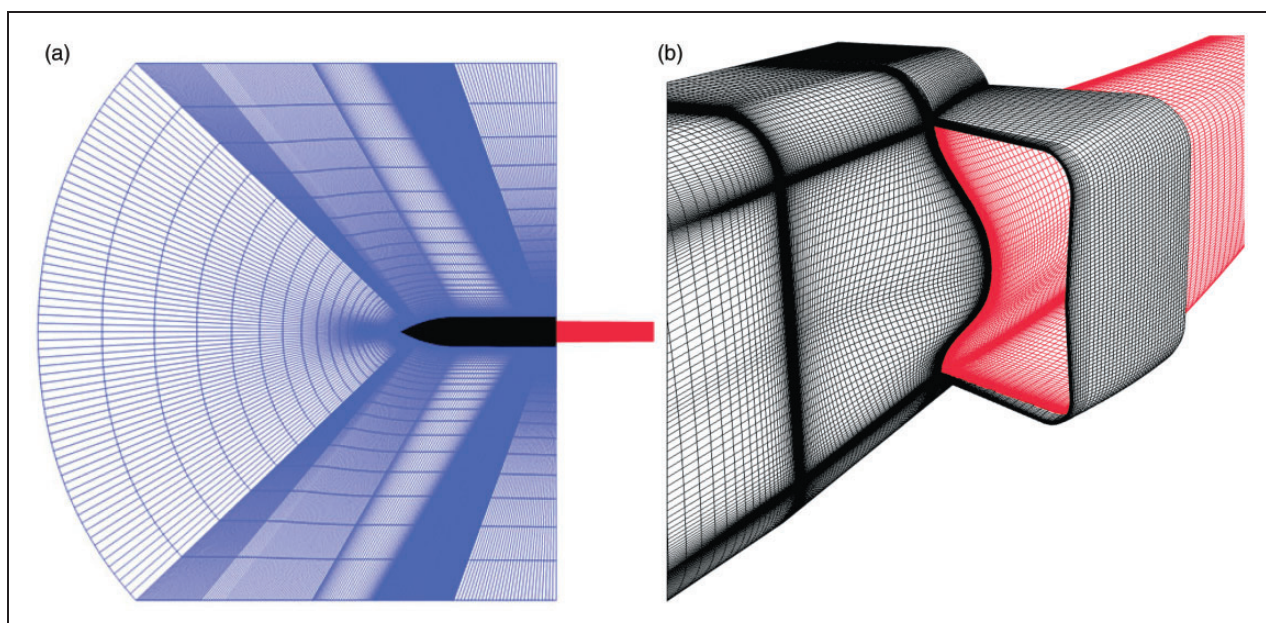


Figure 7. Grid domain for analyzing angle of attack effects. (a) Side view of the forebody-inlet and (b) close-up view of the entrance.

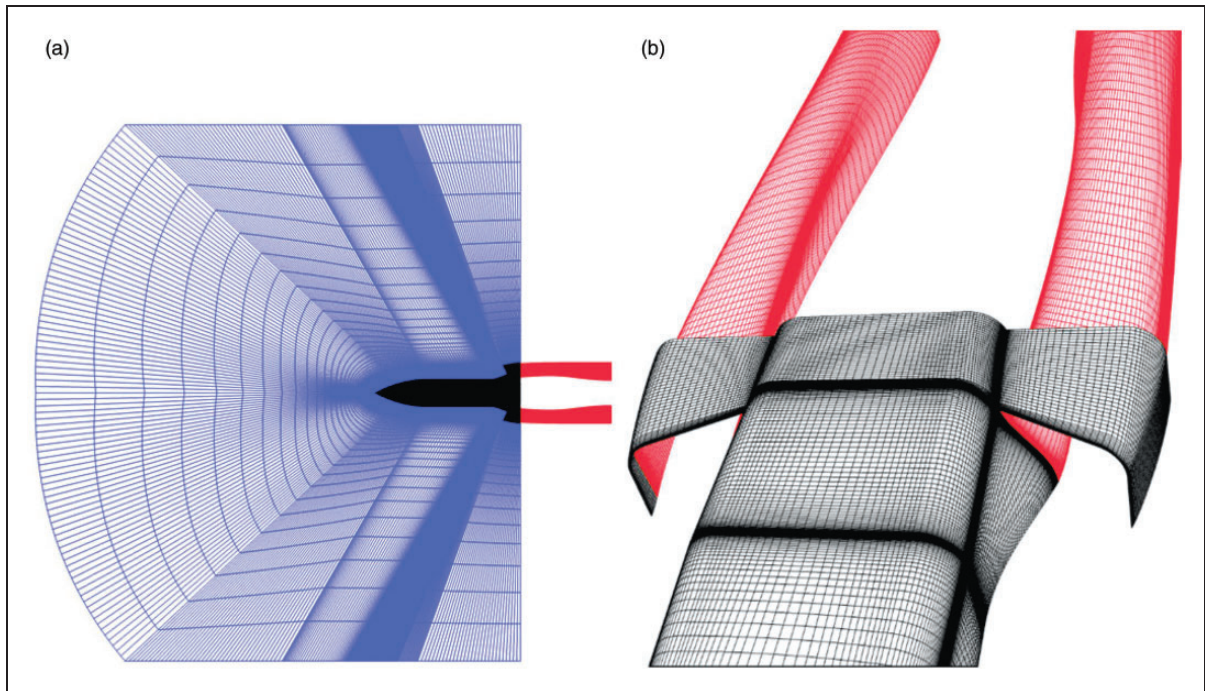


Figure 8. Grid domain for analyzing sideslip angle. (a) Top view of the forebody-inlet and (b) close-up view of the entrances.

outlet boundary condition at the end of the subsonic diffuser with fully structured interior cell blocks. The pressure farfield is big enough to capture the whole nose shock wave. The Mach number, static pressure, and temperature of freestream flow field are 1.60, 79.24 kPa, and 275.15 K for domain initialization.

Governing equations and solver adjustment

The three-dimensional Navier–Stokes equations, coupled with an SST (shear stress transport) turbulence model,²³ are solved by the steady-state upwind algorithm in the domains. The solution starts with the first-order discretization scheme and when the residuals reach 10^{-4} , the solver changes to second-order scheme and continues the iterations with double precision approach.

Analyzing the normal shock wave–boundary layer interactions (NSWBLI), and providing the best prediction about the BL conditions and related phenomena at shock roots, depends on the abilities of the turbulence equations in the numerical solver. The SST turbulence model is used widely in simulations related to viscous interactions. The model is as economical as the $k-\epsilon$ model, but it offers much higher fidelity, especially for separated flows, providing acceptable results in a different range of flows and near-wall mesh conditions. According to our mesh quality and the existence of viscous interactions in our cases, this turbulence model is a good match with the requirements of this analysis. Previous researchers have proven the accuracy of double equation turbulent models for supersonic flow analysis.²³

Table 2. Result of grid study for bump surface.

Grid	Cell number ($\times 10^6$)	U_z
Bump 1	1.1	273.1
Bump 2	2.3	281.0
Bump 3	4.0	282.4

Grid study

A multi-processor system with 40 computational cores solves the multiblock domains using ANSYS Fluent solver, and the convergence is accepted when the residual reaches 10^{-5} . According to the convergence rate of residuals for the DSI, on average more than 8000 iterations are needed. Table 2 summarizes the grid convergence study. For the bump surface, the required cell number is determined by the maximum lateral velocity generated. The accepted grid structure (on the single bump) can also be used for DSI grid generation. The total pressure ratio

$$\sigma = \frac{P_{tAIP}}{P_{t\infty}} \quad (5)$$

on the aerodynamic interface planes (AIPs) (outlets) of the forebody-inlets is used for evaluating the grids. In equation (5), $P_{t\infty}$ is freestream total pressure and P_{tAIP} is the mean total pressure at the AIP. Table 3 summarizes the calculations.

The final grid for forebody-inlet simulations contains about four million cells. The accuracy of the grid structure can also be compared with similar studies in

the study by Saheby et al.²³ The grid domains are interrelated to each other. It means that the grid blocks in Figure 8 are generated by splitting and mirroring the grid blocks in Figure 7, so the grid study of both cases follows a similar cell increment approach.

Results and discussions

Flow pattern of compression surface

The selected compression surface for inlet design in this study generates a set of oblique shock waves which compress the supersonic flow with a smooth pressure increase and lower energy losses as compared with the initial surface in the design process. Figure 9 shows the supersonic pressure coefficient increase of selected bump surfaces along the curve C_s . The maximum U_z on the initial surface is 145.3 m/s and on the final bump is 138.1 m/s. Our CFD data show that the magnitude of U_z variation on the surface of resulting bumps between initial and final bump is 20 m/s with the Reynolds number of 38×10^6 based on the length of wetted area in front of the bump.

A comparison of the pressure rise with a 10° ramp in Figure 9 demonstrates an important characteristic of the role of the bump's nose section. The smooth curvature of the frontal section prevents oblique

shock bifurcation and BL thickening on the bump. The quasi-isentropic shock array delays BL separation and prevents shock bifurcation before the normal shock. In addition, the pressure gradient on the bump surface diverts the BL to the sides of the bump before it has a chance to separate.

Figure 10 shows the resulting flow structure of the bump for the condition of a BL from a flat extension with the same length as the forebody. The oil pattern in Figure 10 shows the BL diversion clearly. Figure 10 also shows Mach number contours on a designated cross-sectional normal plane just before the terminal shock. Mach number varies from about 1.25 at the center to 1.40 over the sides, which matches with the required Mach range for a normal shock. This velocity distribution affects the normal shock structure, subsonic flow spillage, and flow quality inside the subsonic duct. The effects are investigated in section 4.3.

Table 3. Result of grid study for forebody-inlet configuration.

Grid	Cell number ($\times 10^6$)	σ_{AIP}
DSI 1	2.1	0.941
DSI 2	4.1	0.932
DSI 3	7.9	0.929
DSI 4 (independent grid domain)	10.1	0.930

AIP: aerodynamic interface plane; DSI: diverterless supersonic inlet.

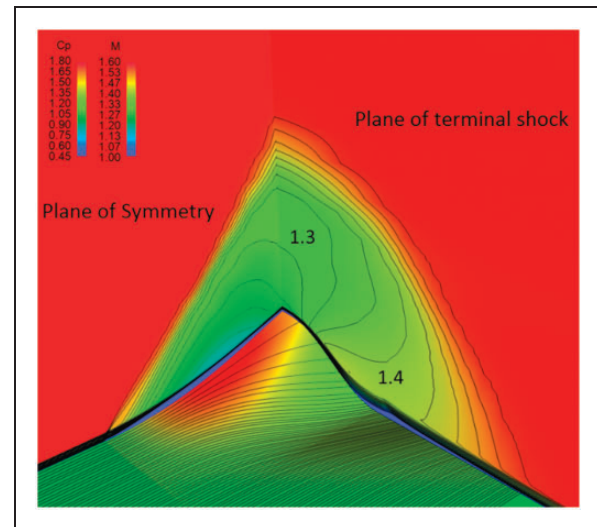


Figure 10. Oil pattern, surface C_p and M for bump surface, $M_\infty = 1.60$.

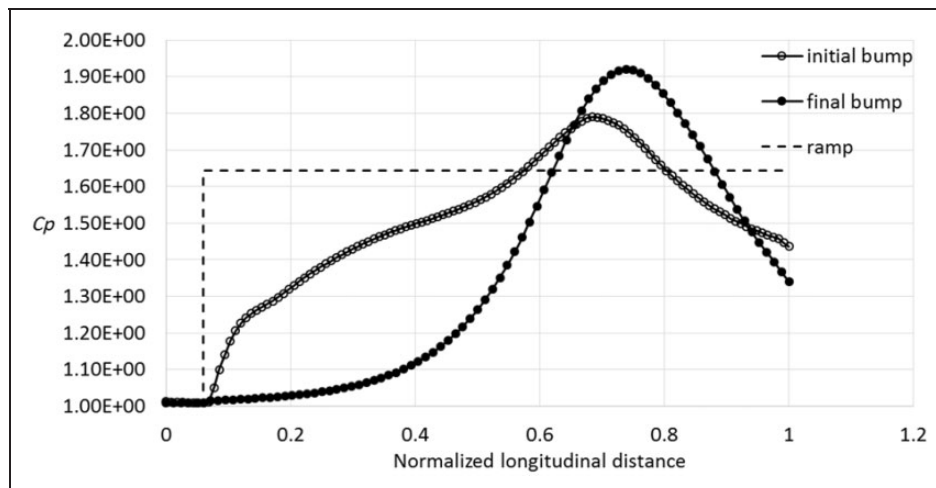


Figure 9. Pressure coefficient along the C_s curve.

BL on the forebody

The fuselage is generated by the transition from a circular cross-section at the nose to a filleted rectangular cross-section. Figure 11(a) to (d) demonstrates the forebody-induced vortices by cross-sectional total pressure ratio contours, vorticity, and tangential streamlines just before the bump at $\alpha=10^\circ$ and $\beta=10^\circ$, respectively. At the condition of sideslip or positive (or negative) angle of attack, the smooth pressure gradient on the rounded corners of the fuselage delays shear layer separation along the transversal direction, so that the vortices tend to move toward the center of the flat section and continue their path along the plane of symmetry. From inspection of the longitudinal vorticity contours, it appears that these vortices are contained within the BL.

Until the vortices are attached to the surface, their interaction with the normal shock wave cannot result in a strong breakdown or shock deformation at the entrance. The interactions are discussed in “Effects of sideslip” section.

Flow pattern of isolated inlets

The DSI shock structures are shown in Figure 12 for the condition in which the wetted area in front of the inlet is negligible. For inlet A, the normal shock near the cowl lip (between the merger of the oblique and normal shocks and the lip) receives a layer of free-stream flow at M_∞ , so that a stronger pressure rise in that area results in the formation of a flow layer with lower kinetic energy. Cross-sectional contours in Figure 12(a) illustrate the internal flow pattern inside the subsonic duct where a low kinetic energy layer is shown on the outboard surface of the duct while inlet B shows a cleaner outboard surface in Figure 12(b). What happens to inlet A is a common problem in external supersonic inlets.²⁴

Due to the transversal velocity (pressure) gradient over the bump, the structure of the normal shock is not planar. Pressure distribution on the bump surface shows the curvature of the terminal shock in the upper half of Figure 13. Yang⁹ reported similar shock structures at the entrance. With no thick BL

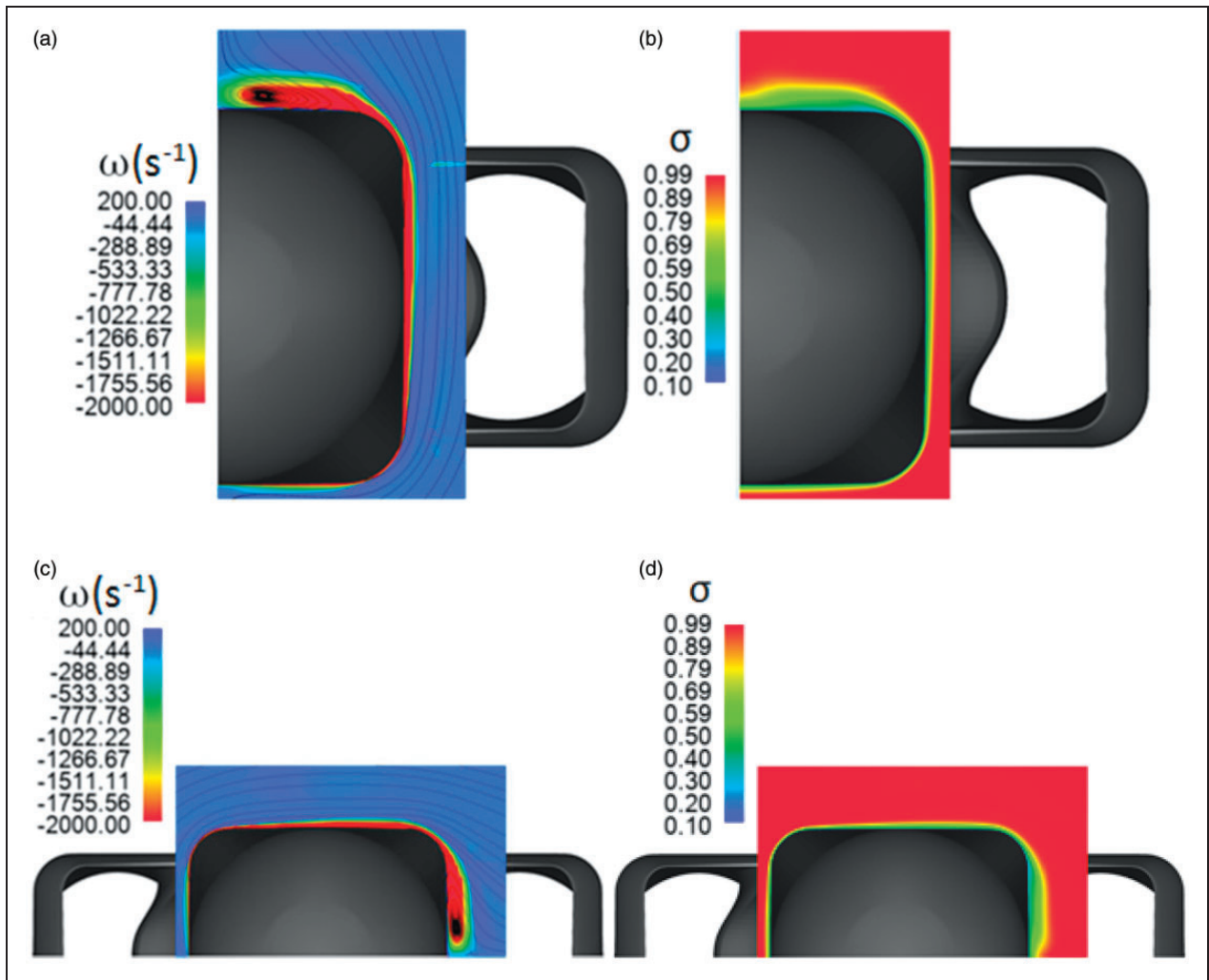


Figure 11. Total pressure ratio and vorticity contour before the bump. (a) Vorticity contour at $\alpha=10^\circ$ and $\beta=0^\circ$, (b) total pressure ratio at $\alpha=10^\circ$ and $\beta=0^\circ$, (c) vorticity contour at $\alpha=0^\circ$ and $\beta=10^\circ$, and (d) total pressure ratio contour at $\alpha=0^\circ$ and $\beta=10^\circ$.

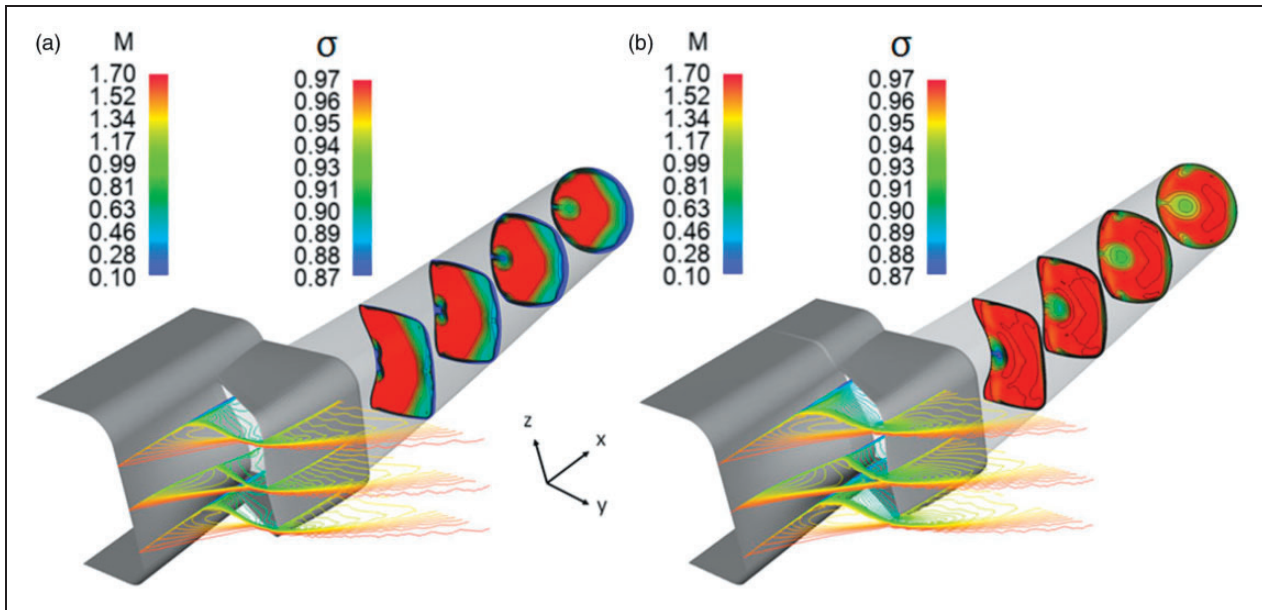


Figure 12. Flow pattern of isolated inlets. (a) Inlet A and (b) inlet B.

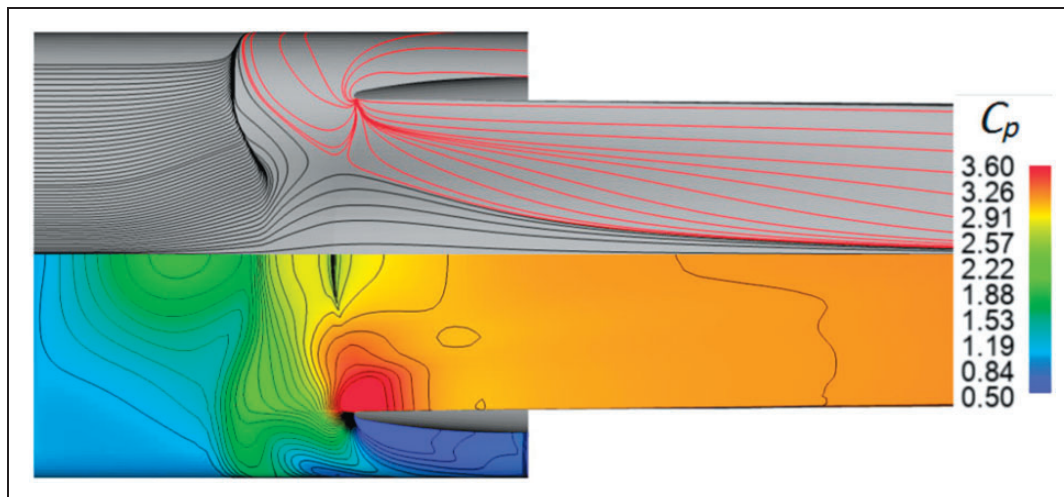


Figure 13. Pressure coefficient distribution and oil pattern on the bump and duct, inlet A, $\alpha = 0.0$, and $\beta = 0.0$.

from upstream, the shock-wave/BL interactions on the bump surface are not strong enough to generate a separating bubble in both cases, and two counter-rotating vortical flow patterns along the plane of symmetry appear inside the ducts. As shown in the lower half of Figure 13, there is a transversal pressure gradient at the shoulder section from the high-pressure zone of the cowl profile to a low pressure zone at the shoulder. The high pressure zone at this location is helpful in pushing the low kinetic energy BL outside the inlet cowl, but it generates a lateral velocity component in a portion of the BL entering the inlet near the cowl profile, so that this layer moves toward the center of the duct. The difference between the velocity vectors of this layer and the BL at the center of the shoulder results in a vortex formation. The black and

Table 4. Supersonic performance of isolated inlets.

Study case	σ_{AIP}	\bar{k}	MFR
A _{isolated} Subcritical	0.937	51.20	0.82
B _{isolated} Subcritical	0.956	35.74	0.68

AIP: aerodynamic interface plane; MFR: mass flow ratio.

red streamlines in the upper half of Figure 13 demonstrate the difference in velocity vectors. The vortices in inlet A are attached to the inboard surface of the duct but in inlet B, they are detached and move toward the center of the AIP.

Table 4 summarizes the total pressure recovery ratio and averaged turbulence kinetic energy \bar{k} on the AIPs. Turbulence kinetic energy is the mean

kinetic energy per unit mass associated with eddies in turbulent flow which can also show the existence of non-uniformity in a subsonic flow field.

In Table 4, the mass flow ratio is calculated by

$$\text{MFR} = \frac{\dot{m}_{AIP}}{\dot{m}_{idal}} \quad (6)$$

In this formula, \dot{m}_{AIP} is the mass flow rate at the AIP and is the \dot{m}_{idal} is the mass flow rate at the throat without any spillage. The performance of the isolated inlets is considered as a baseline for evaluating and comparing the effects of the forebody on the performance of the DSI.

Flow pattern of forebody-inlet configuration

Figure 14 shows an overall view of the flowfield, and Figure 15 compares the flow pattern of the integrated

inlets. At the isolated condition, inlet B shows a better internal flow performance, but on the fuselage, it generates large diameter vortices inside the subsonic diffuser after flow separation at the normal shock root. The intensity of the vortical flow pattern is considerably lower in inlet A where there is no significant flow separation at the throat. This difference is mainly related to the local Mach number above the BL at the normal shock root; for inlet A, with the same back pressure as inlet B, this section receives a flow with $1.22 < M < 1.26$ on the plane of symmetry, but the shock root on inlet B exposes $1.33 < M < 1.37$ because the entrance has shifted back and the transversal velocity gradient before the terminal shock is different. According to Atkin and Squire,²⁵ when the Mach number is greater than 1.30, a lambda-shaped shock root and induced flow separation are unavoidable after NSWBLI and the shock structure of inlet B demonstrates this fact in Figure 16(a). A similar flow

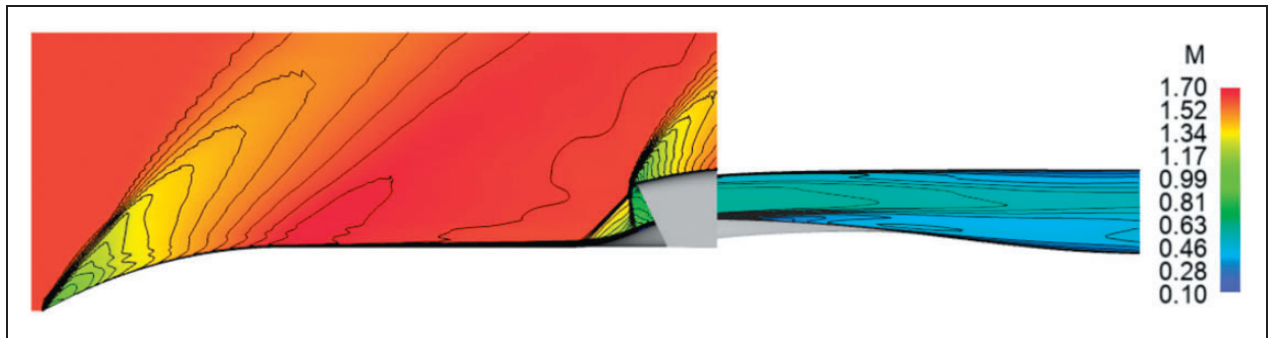


Figure 14. View from underside of Mach contours on the plane of symmetry, inlet A.

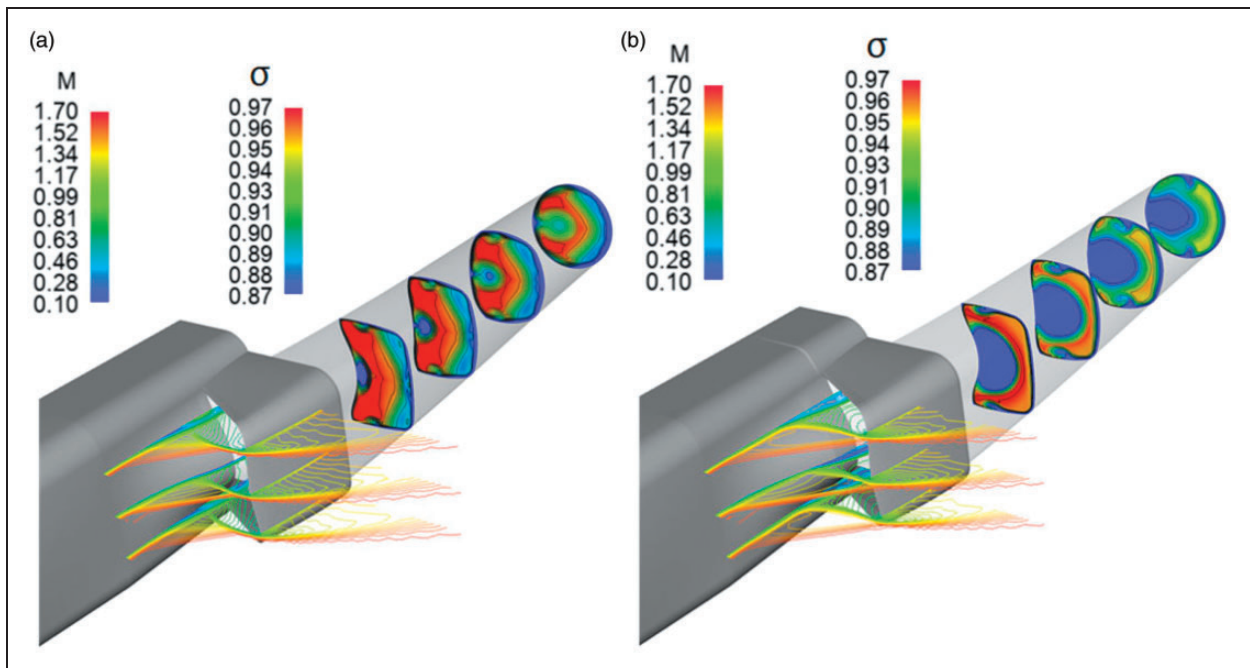


Figure 15. Mach and total pressure contours, $\alpha = 0.0$ and $\beta = 0.0$. (a) Inlet A and (b) inlet B.

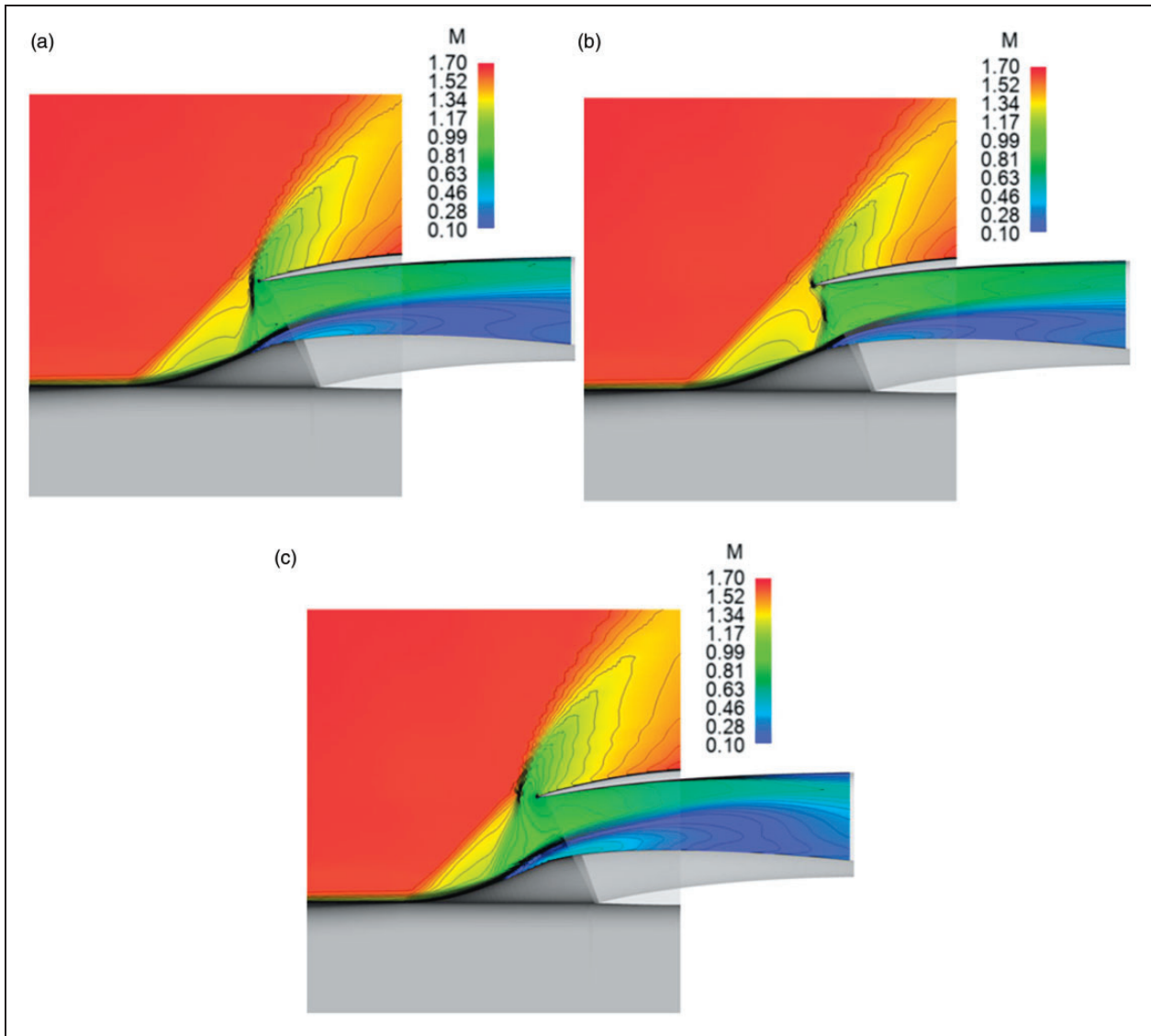


Figure 16. Effect of back pressure on the normal shock of inlet B. (a) No change in back pressure, (b) 5% reduction in back pressure, and (c) 5% increment in back pressure.

separation, started at the throat, is also reported in the study by Masud and Akram¹⁰ (Figure 2(b)). Our study shows that after flow separation, it is not possible for the inlet to recover by changing the back pressure.

Figure 16(b) and (c) demonstrates the effect of back pressure on the Mach contours on the plane of symmetry. From observation of the internal flow patterns, it appears that inlet B cannot reach the requirement of supersonic cruise, so that it is used for angle of attack and sideslip analysis. Table 5 summarizes the efficiency parameters of the installed DSIs, and Table 6 shows a few examples from other sources to compare the efficiency of the current configuration.

For Table 6, note that parameters such as the length of the subsonic diffuser, use of a bleed system, and the structure of cowl lip affect the total pressure recovery. To render a better estimation, the pressure recovery after the normal shock at the shoulder section (σ_s) is also calculated in Table 5.

Table 5. Supersonic performance at cruise condition.

Study case	σ_{AIP}	σ_s	\bar{k}	MFR
A _{install} subcritical mode	0.926	0.943	77.155	0.77
B _{install} subcritical mode	0.891	0.939	276.126	0.67
A _{install} critical mode	0.905	0.918	141.270	0.85
B _{install} critical mode	0.906	0.923	160.093	0.82

AIP: aerodynamic interface plane; MFR: mass flow ratio.

Another effect of upstream BL diversion can be seen on the shape of the terminal shock waves at subcritical mode. At the center of the bump on inlet A, the NSWBLIs are weaker because the thickness of the BL is at a minimum, but at the sides of the bump, where the BL accumulates (Figure 17(a)), the strong interactions form a small separation bubble, so that the terminal shock-front becomes highly curved.

Table 6. Pressure recovery of supersonic inlets for $M \leq 2.0$, $\alpha = 0$, $\beta = 0$.

Inlet type	σ_{AIP}	Cowl lip	Integration/operation	Simulation or test explanations
Parametric DSI ²³	0.94	Sharp	On a cylindrical extension with sharp lips	Second order upwind with SST $k-\omega$
Variable ramps ²⁴	0.94	Profile	On a fuselage with diverter and bleed mechanism	Wind tunnel test, $M_\infty = 1.6$, MFR = 0.6–0.85
DSI ²⁶	0.93–0.91	Profile	Top mounted on a prototype	Wind tunnel test, $M_\infty = 1.45$ –1.55
DSI ³	0.95	Profile	On fuselage with bleed system and side diverter	Wind tunnel test, $M_\infty = 1.5$, MFR = 0.70
Ramp + bump ¹⁶	0.92	Sharp	Isolated inlet	Second order upwind with SST model, $M_\infty = 2.0$
Single Ramp inlet with no side fairing ²¹	0.91	profile	On a fuselage with diverter and bleed surfaces	Wind tunnel test, $M_\infty = 1.5$, MFR = 0.95

MFR: mass flow ratio; SST: shear stress transport; DSI: diverterless supersonic inlet.

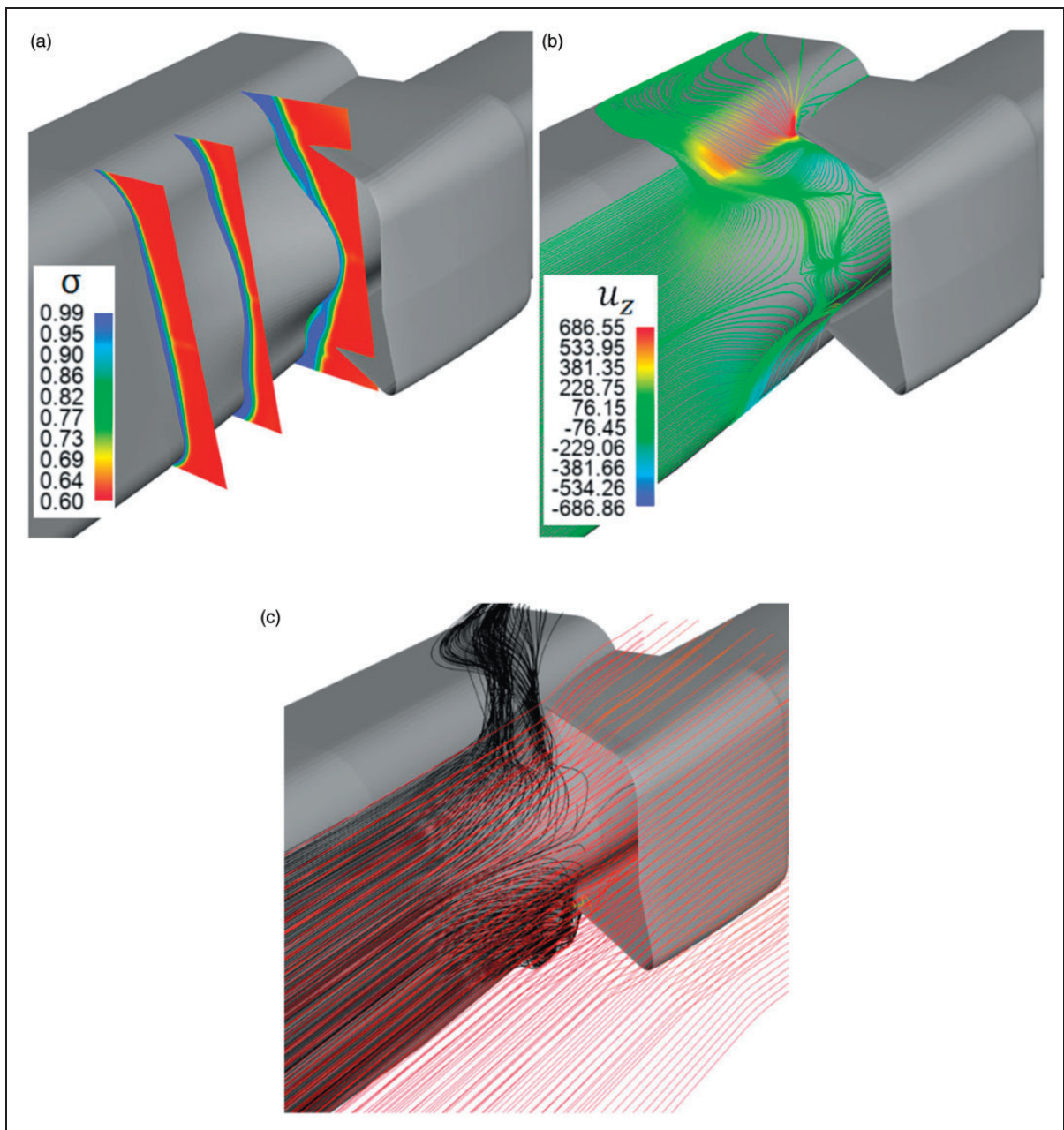


Figure 17. Inlet A flow structure at the entrance. (a) Total pressure ratio contours, (b) surface streamlines, and (c) flowfield streamlines, $\sigma < 0.60$ in black.

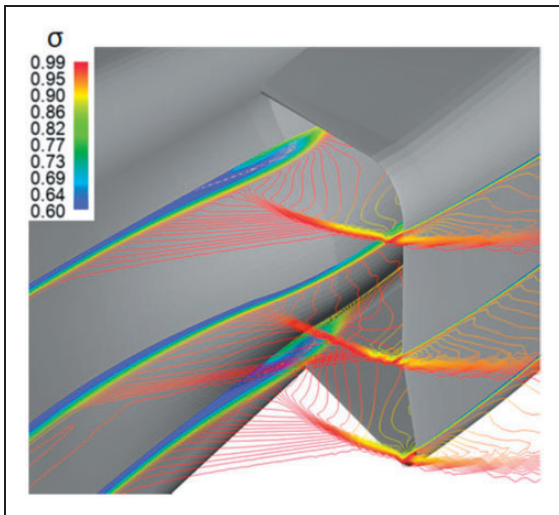


Figure 18. Disappearance of low-energy subsonic layer ($\sigma < 0.6$) after the normal shock.

Such a flow pattern has also been demonstrated in the study by Yang.⁹ The trace of the terminal shock on the surface oil pattern in Figure 17(b) shows this phenomenon. In this figure, the minus sign in u_z indicates the ($-z$) direction of the lateral velocity vector.

The NSWBLI generates a low subsonic velocity flow, chaotic and sensitive to the pressure gradient in the flow structure near the surface just before the entrance (especially at the sides), but the high pressure zone after the normal shock deflects this flow away from the duct at the sides of the entrance. This flow spillage, demonstrated by streamlines in Figure 17(c), reduces the captured mass flow, but it is necessary for recovering the flow quality. The role of the swept forward cowl is to concentrate this spillage at the sides of the entrance. Note that the streamlines with $\sigma < 0.6$ are fully diverted; Figure 18 demonstrates this by observation of the total pressure ratio contours on the plane of symmetry.

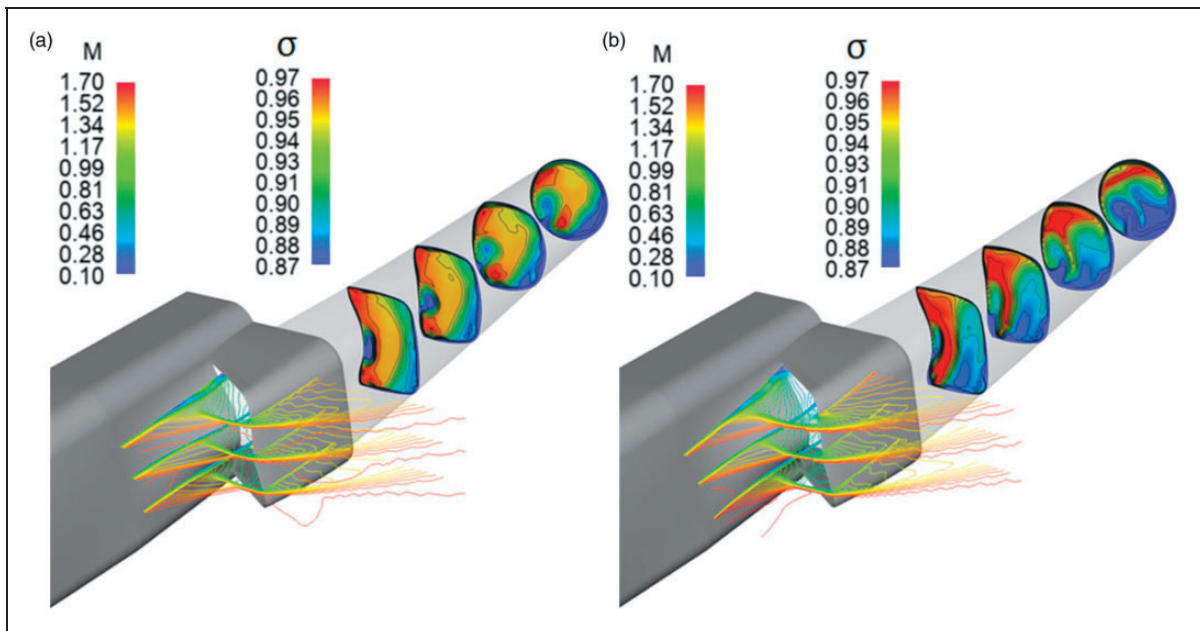


Figure 19. Mach and total pressure contours, inlet A. (a) $\alpha = 5.0^\circ$ and (b) $\alpha = 10.0^\circ$.

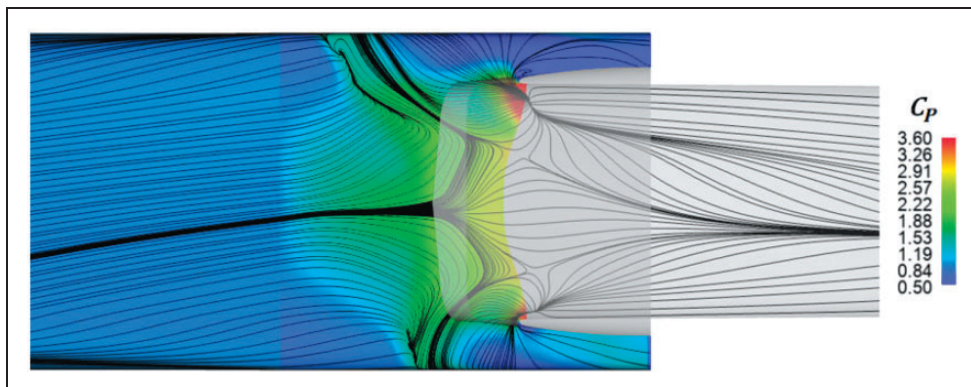


Figure 20. Side view of the surface streamlines inlet A at $\alpha = 5.0^\circ$.

Effects of angle of attack

To study the effects of angle of attack, the velocity vector is changed in the pressure far-field to 5° and 10° from the plane of symmetry. Simulations show that the rotated bump generates a new compression

Table 7. Supersonic performance of inlet A at various angles of attack.

α	σ_{AIP}	σ_s	\bar{k}	MFR
5°	0.922	0.930	71.86	0.76
10°	0.903	0.921	101.42	0.68

AIP: aerodynamic interface plane; MFR: mass flow ratio.

Table 8. Pressure recovery of supersonic inlets for $M \leq 2.0$, $\alpha \neq 0$, $\beta = 0$.

Inlet type	σ_{AIP} at MFR = 0.95	σ_{AIP} at MFR = 0.70
Single Ramp inlet with no side fairing ²⁶	0.91 at $\alpha = 5^\circ$ 0.88 at $\alpha = 9.5^\circ$	0.92 at $\alpha = 5^\circ$ 0.91 at $\alpha = 9.5^\circ$
DSI ³	0.95 at $\alpha = 5^\circ$ 0.92 at $\alpha = 9.3^\circ$	0.96 at $\alpha = 5^\circ$ 0.94 at $\alpha = 9.3^\circ$

MFR: mass flow ratio; DSI: diverterless supersonic inlet.

surface relative to the velocity vector and keeps the oblique and normal shocks in front of the inlet efficiently. Figure 19(a) and (b) shows the inlet A flow pattern at corresponding angles of attack. The contours show that the distortion is mainly because of flow separation at the lower cowl lip. When the swept cowl is used in design, the shear flow separation at the lower lip generates considerably larger diameter vortex.

Although the shock interactions on the fuselage may result in vortex generation, on the current configuration, the DSI can accept an angle of attack of 10° without oblique shock detachment or vortex generation on the bump surface. The normal shock deformation at $\alpha = 5^\circ$ can be seen by its trace on the surface streamlines in Figure 20.

Up to an angle of attack of 5° , the internal flow pattern does not show a serious distortion but at 10° , the domain of the subsonic diffuser is dominated by the chaotic flow patterns. The flow quality factors are summarized in Table 7, and Table 8 provides similar cases for comparison.

Effects of sideslip

The overall flow pattern of the configuration at $\beta = 10^\circ$ is shown in Figure 21 by Mach contours on the plane of symmetry, as viewed from above. The

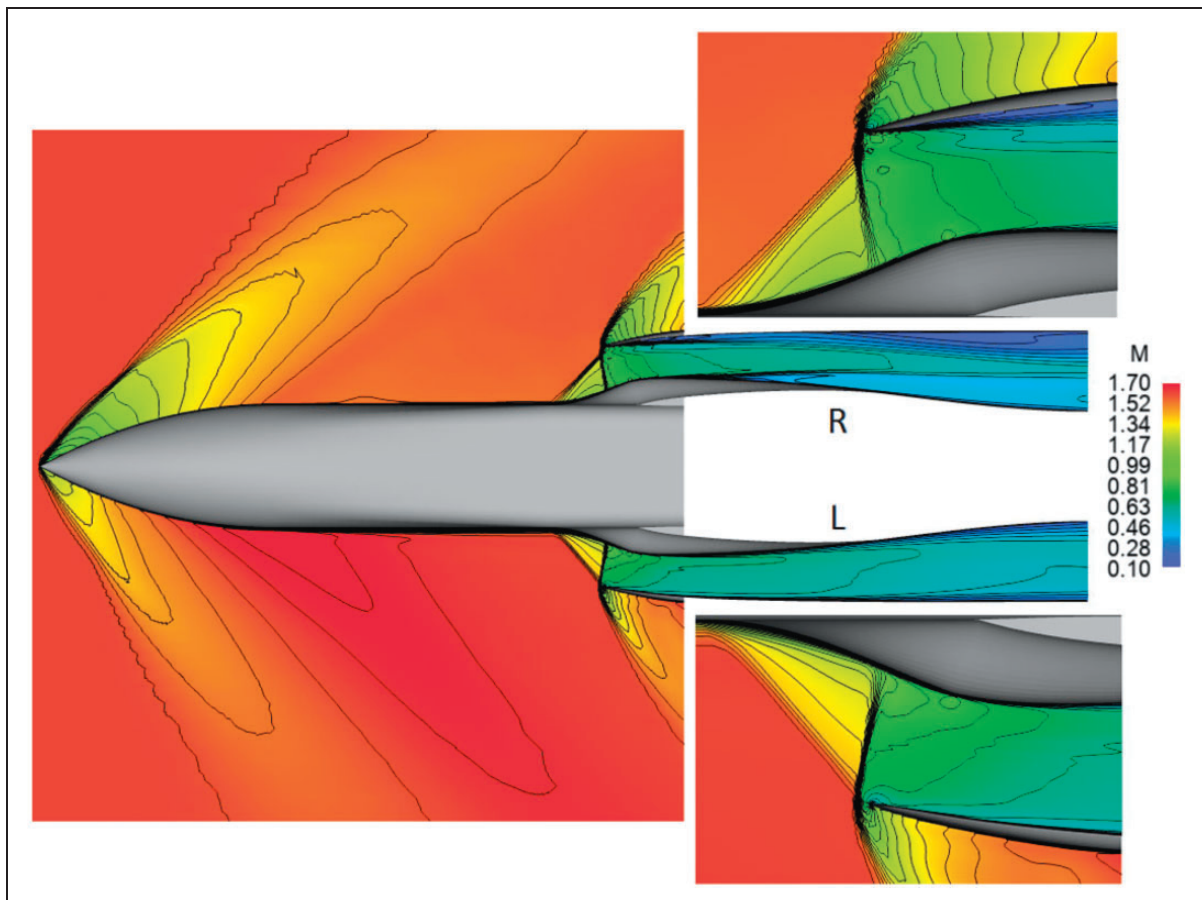


Figure 21. Mach contours on the plane of symmetry, $\beta = 10^\circ$.

inlet on the right side (R) receives a thinner BL and weaker normal shock while the left inlet (L) receives a thicker BL and relatively stronger normal shock. The close-up views on the entrance section show the

differences; the terminal shock on inlet R has shifted forward especially near the shock root. Because the cowl lips are not variable, at high-speeds, sideslip results in flow separation on one of the outboard

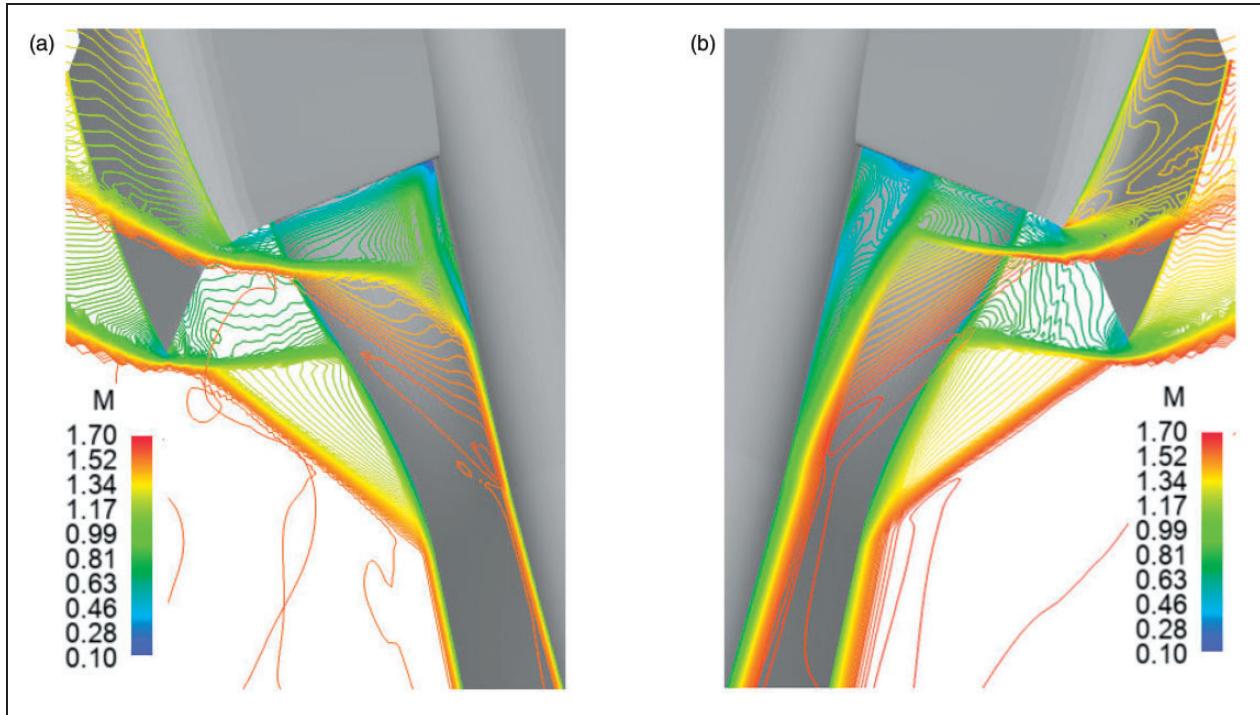


Figure 22. Mach contours at the entrance $\beta = 10^\circ$. (a) R-inlet and (b) L-inlet.

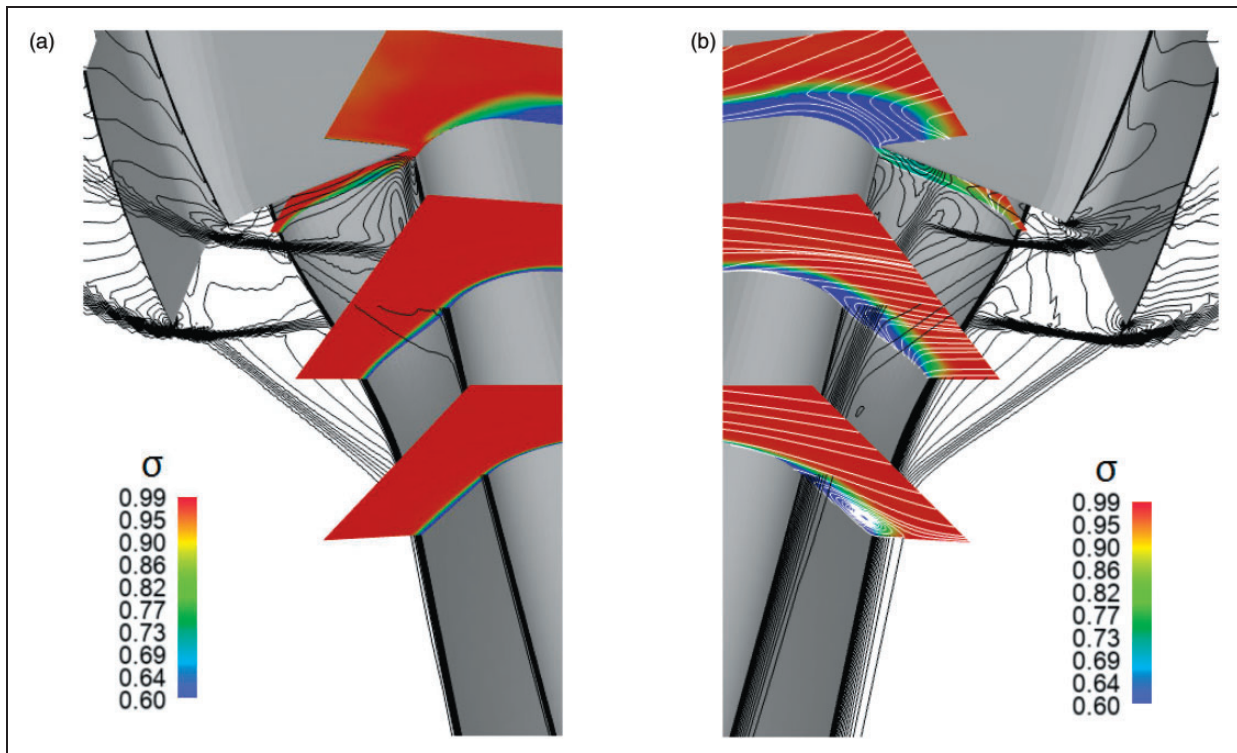


Figure 23. Total pressure ratio contours at $\beta = 10^\circ$. (a) R-inlet and (b) L-inlet.

surfaces of the inlets which is recognizable on inlet R in this figure.

The NSWBL interactions are stronger for the inlet L because of accumulation of the upstream BL before the bump and higher Mach number before the normal

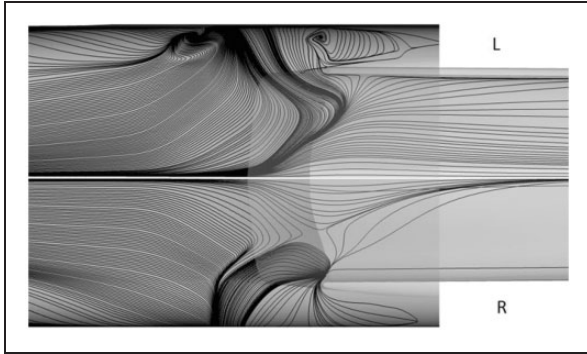


Figure 24. Side view of surface streamlines, The inlet R is inverted. $\beta = 10^\circ$.

shock wave. The longitudinal Mach contours at the entrance of inlet in Figure 22 show a difference between the NSWBLs at the sides of the bumps far from the plane of symmetry. With a thin upstream BL in Figure 22(a), the separation bubbles are not developed, whereas Figure 22(b) demonstrates a large separation bubble at the normal shock root. Although the interactions result in developing a thick subsonic

Table 9. Supersonic performance of inlet A at various sideslip angles.

Inlet/ β	σ_{AIP}	σ_s	\bar{k}	MFR
R/ 5°	0.930	0.946	75.547	0.78
R/ 10°	0.932	0.942	88.253	0.80
L/ 5°	0.927	0.936	134.430	0.79
L/ 10°	0.921	0.932	65.189	0.79

AIP: aerodynamic interface plane; MFR: mass flow ratio.

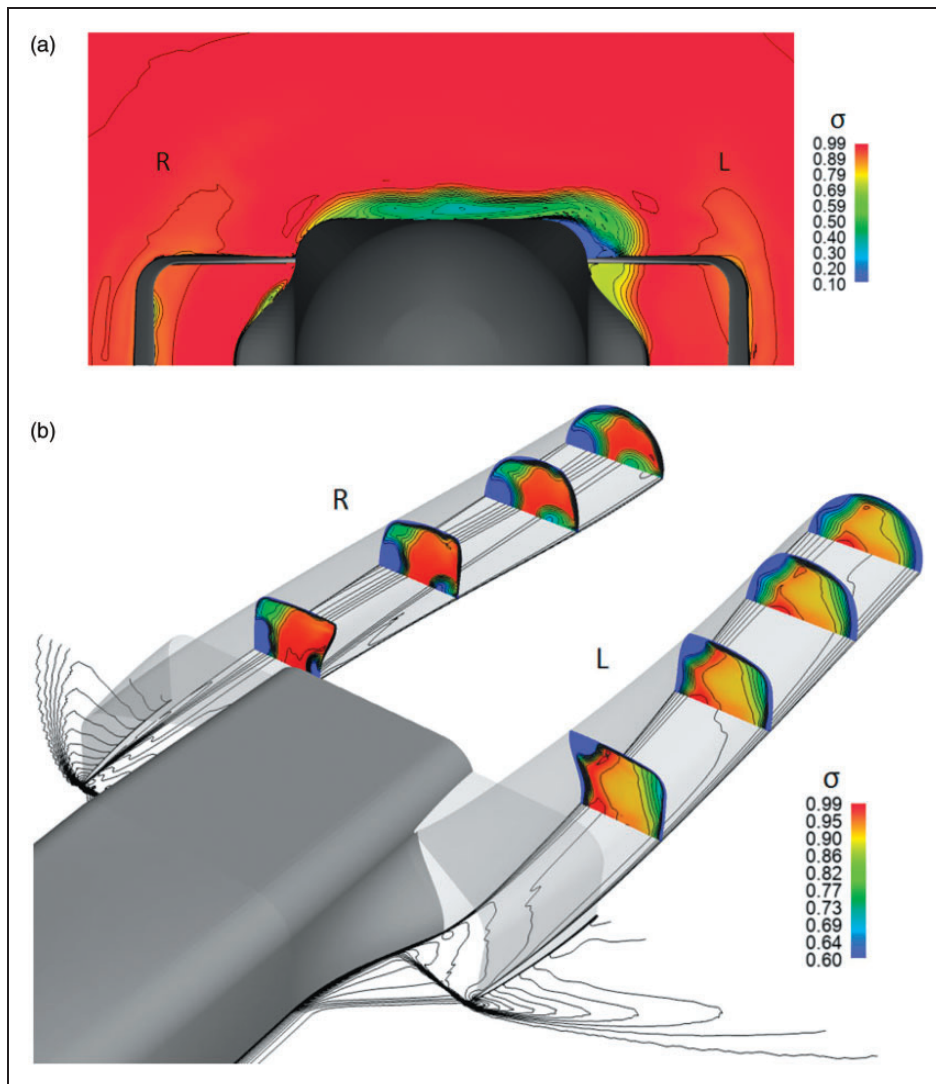


Figure 25. Cross-sectional total pressure ratio contours at $\beta = 10^\circ$. (a) Entrance and (b) inside the duct.

Table 10. Comparison of pressure recovery of supersonic inlets for $M \leq 2.0$ at sideslip conditions.

Inlet type	σ_{AIP}
Single Ramp inlet with no side fairing ²¹	0.82 at $\beta = 6$, MFR = 0.9
	0.84 at $\beta = 6$, MFR = 0.8
DSI ³	0.94 at $\beta = 5$, MFR = 0.8

AIP: aerodynamic interface plane; MFR: mass flow ratio.

layer, side spillage still sends out a considerable portion of the subsonic layers.

Cross-sectional total pressure ratio contours in Figure 23(a) and (b) demonstrate this spillage. The forebody-induced vortices inside the BL disappear, while passing the oblique shock layers with no sudden expansion, strong breakdown, or flow distortion is visualized. Figure 24 shows the difference

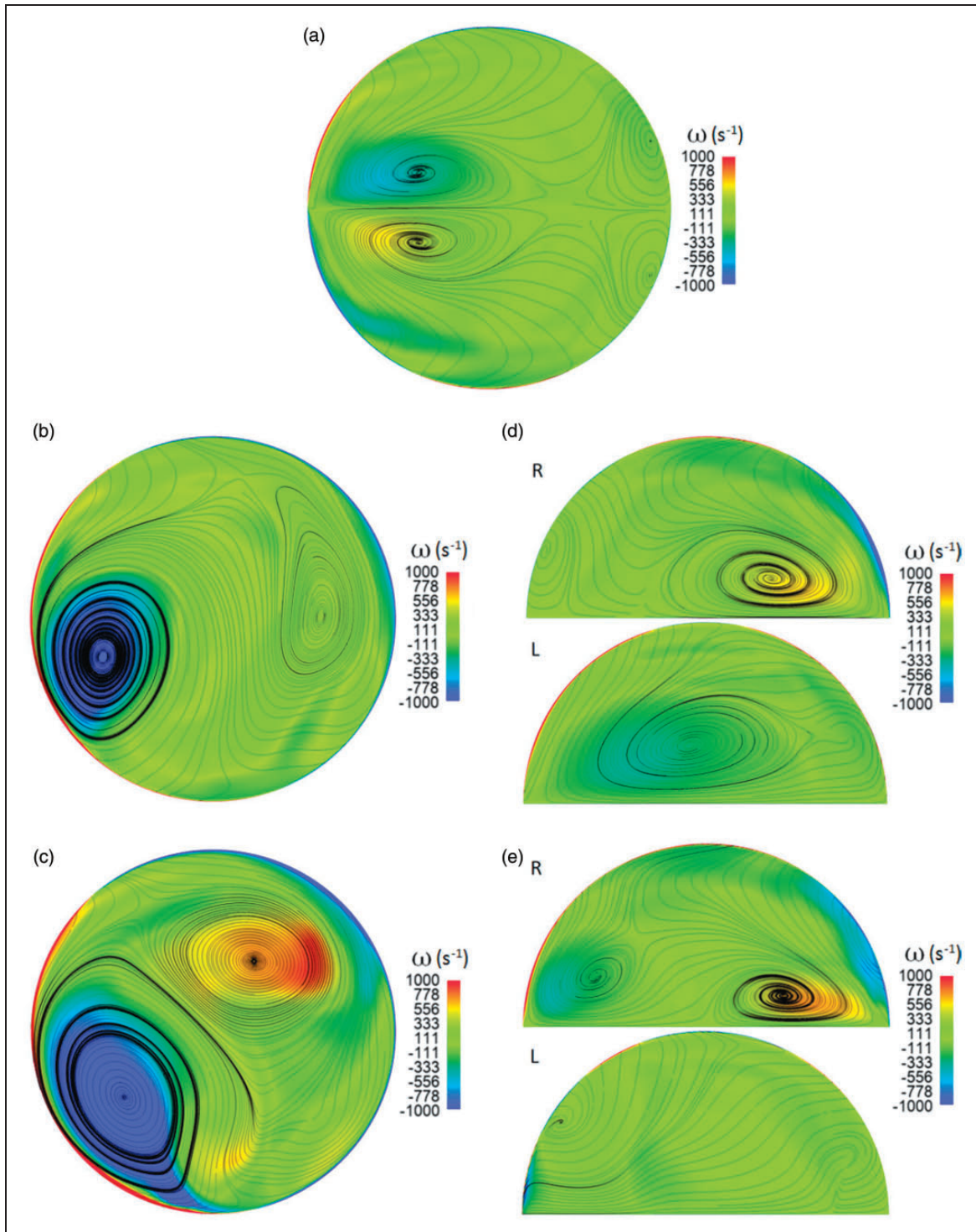


Figure 26. Vorticity on the AIPs. (a) $\alpha = 0.0^\circ$ and $\beta = 0.0^\circ$, (b) $\alpha = 5.0^\circ$ and $\beta = 0.0^\circ$, (c) $\alpha = 10.0^\circ$ and $\beta = 0.0^\circ$, (d) $\alpha = 0.0^\circ$ and $\beta = 5.0^\circ$, and (e) $\alpha = 0.0^\circ$ and $\beta = 10.0^\circ$.

between the normal shock interactions on the bump surfaces by oil patterns on the compression surfaces, shown here with transparent cowls and diffuser ducts. Figure 25(a) shows the diverted flow total pressure ratio contours at the entrance, and Figure 25(b) illustrates the internal flow patterns in the subsonic diffusers.

Because of the similarity between the flow patterns of inlets at 5° and 10° of sideslip, the contours and images related to of $\beta = 10^\circ$ are presented in this section. Flow quality factors are also measured for $\beta = 5^\circ$. Table 9 summarizes the calculations, and Table 10 shows the result of analysis of similar inlets for comparison.

The importance of the bump's shock structures at sideslip can be understood by comparing it with a fixed wedge (double shock) inlet; if the ramp angle is equal to 8° (to reduce the supersonic flow to Mach 1.30), then exceeding 7° angle of attack on an aircraft such as the Eurofighter Typhoon results in shock detachment on the wedge for a chin inlet configuration.

Vorticity measurement at AIP

The longitudinal vorticity (ω) at the outlet of the study cases is shown in Figure 26, which demonstrates the flow structure at the AIPs by the tangential streamlines.

The minus sign corresponds to counter clockwise rotation. Comparing the magnitude of vorticity between cases permits comparison of the performance of the duct designs. The AIPs show that the current DSI configuration has a more reliable pattern in sideslip in comparison with angle of attack, mainly because of cowl design. The current cowl results in the formation of large diameter vortices at significant angles of attack.

Conclusion

This work demonstrates the potential of CFD-based-design compression surfaces for a DSI application. In this research, a three-dimensional bump surface is designed by CFD simulation iteratively and used in designing a side-mounted supersonic inlet on a generic fuselage. Two cowl structures for subcritical operation are developed and the inlet with the higher internal aerodynamic performance at the installed condition is selected for angle of attack and sideslip analysis. Results illustrate the following:

1. The installed total pressure recovery of the selected DSI is in the range of other supersonic inlets. The total pressure recovery and mass flow capture ratio of the installed system at cruise speed is reduced 1.7% and 6.1% compared to an isolated model based on the $k-\omega$ turbulence model. The DSI operates based on subsonic flow spillage at the sides of the bump, which reduces the mass

flow capture ratio when compared with a more conventional inlet with BL diverter.

2. DSI entrance diverts a portion of upstream BL with the local total pressure ratio less than 0.60. The distance between the normal shock and the cowl lip provides a high pressure zone to divert the subsonic flow. Studying the flow pattern of the inlet with forebody effects shows the consistency of the DSI's shock structure up to 10° angle of attack and sideslip, which is considerably better in comparison with the other two-dimensional inlets.
3. The rotated bump surface generates a set of oblique shock waves which result in a pressure recovery of about 0.92 at different angles of attack and sideslip up to 10° . The flow diversion process is still present at these angles. The flow quality inside the subsonic duct shows an acceptable pattern up to 10° of sideslip but at 10° angle of attack, vortical structures occupy most of the duct volume.

CFD analysis shows that the inlet has sufficient capability to ensure operation during maneuvers at the design speed, especially if the cowl structure is optimized for such maneuvers and flow control technology has been applied to improve the internal flow pattern.

Acknowledgement

The authors gratefully acknowledge the research support of the College of Aerospace in Nanjing University of Aeronautics and Astronautics.

Declaration of Conflicting Interests

The author(s) declared no potential conflicts of interest with respect to the research, authorship, and/or publication of this article.

Funding

The author(s) disclosed receipt of the following financial support for the research, authorship, and/or publication of this article: The research team is supported by the National Natural Science Foundation of China (No. 11872207).

ORCID iD

Eiman B Saheby  <https://orcid.org/0000-0001-7153-3427>

References

1. Tillotson BK and Loth E. Experimental study of a Mach 3 bump-compression flowfield. *J Propul Power* 2009; 25: 545–554.
2. Lo KH, Zare-Behtash H and Kontis K. Control of flow separation on a contour bump by jets in a Mach 1.9 free-stream. *Acta Astronautica* 2016; 126: 229–242.
3. Simon PC, Brown DW and Huff RG. *Performance of external-compression bump inlet at Mach numbers of 1.5 and 2.0*. NACA Report NACA-RM-E56L19, 24 April 1957. Washington, DC: National Advisory Committee for Aeronautics.

4. Seddon J and Goldsmith EL. Intake Aerodynamics. In: *AIAA education series*. 2nd ed. Reston, VA: American Institute of Aeronautics and Astronautics, 1999, pp.338–340.
5. Ferri A. Scoop-type supersonic inlet with precompression surface. Patent 2990142, USA, 1961.
6. Hamstra JRW. System and method for diverting boundary layer air. Patent 5779189, USA, 1998.
7. Lundy BF and Klinge JD. System, method and apparatus for streamline traced, mixed compression inlets for aircraft engine. Patent 7207520B2, USA, 2007.
8. Saheby EB, Huang GP and Hays A. Design of hypersonic forebody with submerged bump. *Proc IMechE, Part G: J Aerospace Engineering* 2018; 233: 3153–3169.
9. Yang YK. Design of bump inlet of thunder /JF-17 aircraft. *J Nanjing Univ Aeronaut Astronaut* 2007; 39: 449–452.
10. Masud J and Akram F. Flow field and performance analysis of an integrated diverterless supersonic inlet. In: *48th AIAA aerospace sciences meeting*, Orlando, FL, 4–7 January 2010.
11. Hassan JSM, Masud J and Khan O. Intake and airframe characterization through composite CFD. In: *53th AIAA aerospace sciences meeting*, Kissimmee, FL, 5–9 January 2015.
12. Diverterless Supersonic Inlet (DSI), <https://www.globalsecurity.org/military/systems/aircraft/dsi.htm> (accessed 26 January 2019).
13. Svensson M. *A CFD investigation of a generic bump and its application to a diverterless supersonic inlet*. MS Thesis, Linköping University, Sweden, 2008.
14. Kim SD and Song DJ. Numerical study on performance of supersonic inlets with various three-dimensional bumps. *J Mech Sci Technol* 2008; 22: 1640–1647.
15. Kim SD. Aerodynamic design of a supersonic inlet with a parametric bump. *J Aircraft* 2009; 46: 198–202.
16. Kim SD. A computational study on the influence of a bleed slot on the flowfield of a bump-type inlet. *J Mech Sci Technol* 2015; 29: 5245–5250.
17. Han XL. Quadratic trigonometric polynomial curves with a shape parameter. *J Comput Aid Geom Des* 2002; 19: 503–512.
18. Liu HY, Li L and Zhang DM. Study on a class of TC Bezier curve with shape parameters. *J Inf Comput* 2011; 8: 1217–1223.
19. Loth E, Babinsky H, Titchener N, et al. A canonical normal SBFI flow relevant to external compression inlets. In: *51st AIAA aerospace sciences meeting including the new horizons forum and aerospace exposition*, Grapevine, TX, 7–10 January 2013.
20. Xu SC, Wang Y, Wang ZG, et al. The design and analysis of bump in high speed supersonic flow. In: *21st AIAA international space planes and hypersonics technologies conference*, Xiamen, China, 6–9 March 2017.
21. Davids J, George A and Wise GA. *Investigation at Mach numbers 1.5 and 1.7 of twin-duct side intake system with two-dimensional 6° compression ramps mounted on a supersonic airplane*. NACA Report NACA-RM-E53H19, 12 October 1953. Washington, DC: National Advisory Committee for Aeronautics.
22. Gillen T and Loth E. Simulations and experiments of a dual-stream low-boom supersonic inlet. *J Propul Power* 2015; 31: 1567–1577.
23. Saheby EB, Huang GP and Hays A. Design of top mounted supersonic inlets for a cylindrical fuselage. *Proc IMechE, Part G: J Aerospace Engineering* 2018; 233: 2956–2979.
24. Watanabe Y, Ueno A and Murakami A. Design of top mounted supersonic inlet for silent supersonic technology demonstrator S3TD. In: *27th International congress of the aeronautical sciences*, Nice, France, 19–24 September 2010, pp.2764–2772.
25. Atkin CJ and Squire LC. A study of the interaction of a normal shock wave with a turbulent boundary layer at Mach numbers between 1.30 and 1.55. *Eur J Mech B Fluid* 1992; 11: 93–118.
26. Castner RS, Simerly S and Rankin M. Supersonic inlet test for a quiet supersonic transport technology demonstrator in the nasa glenn 8-foot by 6-foot supersonic wind tunnel. In: *2018 Applied Aerodynamics Conference*, Atlanta, Georgia, 25–29 June 2018.

Appendix

Notation

C_{c_1} to C_{c_5}	cross-sectional curves
C_s	bump central guide curve
k	turbulence kinetic energy
\bar{k}	averaged turbulence kinetic energy at AIP
\dot{m}_{AIP}	calculated mass flow rate at the AIP
M	Mach number
M_∞	freestream Mach number
p_1 to p_4	control points
P	static pressure
P_t	total pressure
P_{tAIP}	mean total pressure at the AIP
$P_{t\infty}$	freestream total pressure
U_z	lateral velocity component
$x_{P_{n-Cn}}$ and $y_{P_{n-Cn}}$	coordinates of control point in x-y plane
α	angle of attack
β	sideslip angle
σ	local total pressure ratio
σ_{AIP}	total pressure ratio on AIP
ω	turbulence dissipation rate
ω_x	longitudinal vorticity